AIAA 2001-0725

Isolating Curvature Effects in Computing Wall-Bounded Turbulent Flows

Christopher L. Rumsey and
Thomas B. Gatski
NASA Langley Research Center
Hampton, Virginia

39th AIAA Aerospace Sciences Meeting & Exhibit
8-11 January 2001/Reno, NV

AIAA-2001-0725

ISOLATING CURVATURE EFFECTS IN COMPUTING WALL-BOUNDED TURBULENT FLOWS

Christopher L. Rumsey* and Thomas B. Gatski†
NASA Langley Research Center
Hampton, Virginia

Abstract

The flow over the zero-pressure-gradient So-Mellor convex curved wall is simulated using the Navier-Stokes equations. An inviscid effective outer wall shape, undocumented in the experiment, is obtained by using an adjoint optimization method with the desired pressure distribution on the inner wall as the cost function. Using this wall shape with a Navier-Stokes method, the abilities of various turbulence models to simulate the effects of curvature without the complicating factor of streamwise pressure gradient can be evaluated. The one-equation Spalart-Allmaras turbulence model overpredicts eddy viscosity, and its boundary layer profiles are too full. A curvature-corrected version of this model improves results, which are sensitive to the choice of a particular constant. An explicit algebraic stress model does a reasonable job predicting this flow field. However, results can be slightly improved by modifying the assumption on anisotropy equilibrium in the model's derivation. The resulting curvature-corrected explicit algebraic stress model possesses no heuristic functions or additional constants. It lowers slightly the computed skin friction coefficient and the turbulent stress levels for this case (in better agreement with experiment), but the effect on computed velocity profiles is very small.

1 Introduction

It has long been recognized that many turbulence models in use today are incapable of producing correct physical behavior near curved surfaces. Much of this information comes from the use of boundary-layer codes (e.g., see Wilcox[1]) applied to curved flows with near-zero pressure gradient (e.g., So and Mellor,[2] Gillis and Johnston[3]). The few applications of Navier-Stokes codes to curved wall-bounded flows have generally been for cases with substantial pressure gradients, such as the U-duct test case of Monson and Seegmiller.[4] The use of a test case with pressure gradient can complicate the analysis by making it difficult to isolate the effects of curvature from the effects of pressure gradient. Also, in the Monson and Seegmiller case, one must contend with boundary layer separation and consequently a loss of two-dimensionality.

The reason why Navier-Stokes codes have not been applied to zero-pressure-gradient cases (such as the So and Mellor case) is that in these experiments the outer wall shape has not been explicitly documented. The only information recorded is that the outer wall was manually adjusted during the experiment to yield the desired (near-zero) pressure gradient along the inner curved wall. Additionally, in the case of So and Mellor, a local tangential jet was used at the outer wall near the start of the curve to maintain attached flow on this wall; while in the case of Gillis and Johnston, local boundary layer bleeding accomplished the same thing. From the standpoint of boundary layer methods, this information was adequate. However, these issues produce a significant challenge for the modeling of the entire two-wall setup, as is required in a Navier-Stokes simulation, and preclude a large amount of experimental data from being utilized.

Today, with advances made in optimization methods in CFD, it is now possible to find an outer wall shape that yields a specified pressure distribution on the inner wall. As a result, Navier-Stokes simulations can be relatively easily accomplished on test cases for which boundary layer codes were the only viable option in the past.

In previous work,[5] three turbulence models were used to investigate the U-duct flow of Monson and Seegmiller. The three models employed were the one-equation Spalart-Allmaras (SA),[6] two-equation Menter shear-stress transport (SST),[7] and two-

*Senior Research Scientist, Computational Modeling and Simulation Branch, Associate Fellow AIAA.

†Senior Research Scientist, Computational Modeling and Simulation Branch.

equation explicit algebraic stress model (EASM).[8] All models behaved similarly in the curved region, and all failed to predict the suppression of the turbulent shear stress caused by the convex curvature. Overall, the EASM was judged to be superior to the other two models for this flow field. However, as mentioned above, it is difficult to isolate the effects of curvature from other effects in the Monson and Seegmiller case.

In the present study, we employ two of the above turbulence models (SA and EASM) to the So and Mellor case, which removes the complications of pressure gradient and boundary layer separation from consideration. Both of these turbulence models include recently-developed curvature corrections, and can be run both with and without the corrections in place. We first describe an optimization method used to determine the outer wall shape, given the So and Mellor experimental inner wall pressure distribution. We then apply a Navier-Stokes code to the case. We attempt to answer the following questions regarding the isolated effect of curvature in zero-pressure-gradient flow: (1) how well do existing models *without* curvature correction handle convexly-curved wall-bounded flow? (2) what aspects of the flow are missed, and how significant are the missed effects? (3) how much improvement is gained by employing curvature correction terms to the turbulence models?

2 The Optimization Method

The optimization method is described in Anderson and Bonhaus[9] and Nielsen and Anderson.[10] In summary, a fully discrete adjoint approach is used in an unstructured-grid framework to compute design sensitivities using either the Euler or the Navier-Stokes equations. The adjoint method includes the effects of the interior mesh sensitivities. A quasi-Newton optimization technique, referred to as KSOPT,[11] is currently employed.

In the adjoint approach for design optimization, a cost function is defined and augmented with the flow equations as constraints. In the present case, the cost function to be minimized is the pressure distribution on the inner wall, which is taken from experimental data. The shape of the outer wall is parameterized with 28 design variables. To avoid having to contend with boundary layer separation along the outer wall, the optimization is conducted using the Euler equations and the method is run until the cost function reaches a suitable level of convergence.

3 Numerical Method and Turbulence Models

The Navier-Stokes CFD code used in the current investigation is CFL3D,[12] a widely-used structured-grid upwind finite-volume method. Details about the code can be found in the User's Manual referenced.

The two turbulence models used are the one-equation Spalart-Allmaras (SA) model[6] and the two-equation explicit algebraic stress model (EASM).[5] However, note that the EASM has an additional minor modification, described in Gatski and Rumsey.[13] Equation (4) in Ref. 5 is replaced by:

$$g = \left[\gamma_0^* \frac{\mathcal{P}}{\varepsilon} + \gamma_1^*\right]^{-1}, \tag{1}$$

where

$$\gamma_0^* = \gamma_0 - 1 \tag{2}$$

and

$$\gamma_1^* = \gamma_1 + 1 + \left(\frac{C_{\varepsilon 2} - C_{\varepsilon 1}}{C_{\varepsilon 1} - 1}\right). \tag{3}$$

Gatski and Rumsey[13] showed that a source of error in the EASM for curved flows was caused by the assumption of anisotropy equilibrium in the Cartesian frame of reference in the derivation of the model directly from the full Reynolds stress model:

$$\frac{Db_{ij}}{Dt} = 0, \tag{4}$$

where $b_{ij} = \tau_{ij}/(2K) - \delta_{ij}/3$ and $K = \tau_{nn}/2$ is the turbulent kinetic energy.

In the study of non-Newtonian constitutive relations (e.g., Schunk and Scriven,[14] Souza Mendes et al.[15]), a measure of relative rotation rate is based on the principal axes of the strain rate tensor. By assuming a transformed form of Eq. (4) to hold in this principal axes frame, a new form of the EASM can be derived that takes into account the flow field curvature. This new form is termed EASM curvature-corrected (EASMCC).

In the transformed coordinate frame, the following equation holds:

$$\frac{D\bar{b}_{ij}}{Dt} = 0, \tag{5}$$

where $\bar{b}_{ij}$ is the transformed anisotropy tensor. Written in the Cartesian frame, Eq. (5) becomes:

$$\frac{Db_{ij}}{Dt} = b_{ik}\Omega_{kj} - \Omega_{ik}b_{kj}. \tag{6}$$

The Ω_{ij} tensor is related to the rate of rotation between the principal axes (barred) system and the Cartesian (unbarred) system.

The method for implementation of EASMCC in 2-D is as follows. The rotation rate tensor $W_{ij} = (\partial u_i/\partial x_j - \partial u_j/\partial x_i)/2$ in the model is replaced by an "effective" $W^*_{ij} = W_{ij} - \Omega_{ij}/a_2$, where the constant a_2 is defined by the pressure-strain correlation model. For the SSG model[16] used here, $a_2 = (2 - C_4)/2$ and $C_4 = 0.4$. The tensor Ω_{ij} is given by

$$\Omega_{ij} = \begin{bmatrix} 0 & D\alpha/Dt \\ -D\alpha/Dt & 0 \end{bmatrix}, \tag{7}$$

and $D\alpha/Dt$ is the Lagrangian derivative of the strain-tensor principal axes, given by

$$\frac{D\alpha}{Dt} = \frac{D}{Dt}\left(\tan^{-1}\left[\frac{\sqrt{S_{11}^2 + S_{12}^2} - S_{11}}{S_{12}}\right]\right), \tag{8}$$

where $S_{ij} = (\partial u_i/\partial x_j + \partial u_j/\partial x_i)/2$. This expression can be reduced to (see Ref. 17)

$$\frac{D\alpha}{Dt} = \frac{1}{2(S_{11}^2 + S_{12}^2)}\left[S_{11}\frac{DS_{12}}{Dt} - S_{12}\frac{DS_{11}}{Dt}\right]. \tag{9}$$

In practice, a term is added to the denominator of Eq. (9) to avoid division by zero as well as to avoid spurious fluctuations in $D\alpha/Dt$ in regions of very low gradient. Note that for a simple 2-D azimuthal flow with only a u_θ component of velocity (a function of radius), the following relation can be derived:

$$\frac{D\alpha}{Dt} = \frac{1}{2}(S - W)\text{sign}(W_{12}), \tag{10}$$

where $S = \sqrt{2S_{ij}S_{ij}}$ and $W = \sqrt{2W_{ij}W_{ij}}$. This analytical function can be shown to hold in general only for $\mathcal{R}^2$ very close to 1, where $\mathcal{R}^2$ is defined by

$$\mathcal{R}^2 = -\frac{\{\mathbf{W}^2\}}{\{\mathbf{S}^2\}} \tag{11}$$

and $\{\}$ represents the trace: $\{\mathbf{W}^2\} = W_{ij}W_{ji} = -W_{ij}W_{ij}$ and $\{\mathbf{S}^2\} = S_{ij}S_{ji} = S_{ij}S_{ij}$. Eq. (10) has proved to be useful as a check (in regions where $\mathcal{R}^2 \approx 1$) on the more complicated numerics required to obtain $D\alpha/Dt$ exactly, but it is of limited use in general. We use the exact $D\alpha/Dt$ term given by Eq. (9) for all the results in this paper.

A curvature correction for the SA model has been developed by Spalart and Shur,[17] and applied to a variety of flows in Shur et al.[18] This correction, Spalart-Allmaras for Rotation/Curvature (SARC) was similarly derived based on the rate of change of the principal axes of the strain rate tensor, but it also includes a heuristic function f_{r1} (that multiplies the model's production term), which is not present in the EASMCC.

In the current implementation of the SARC model, $c_{b1}[1 - f_{t2}]W\tilde{\nu}$, a portion of the SA model's production term, is replaced by $c_{b1}[f_{r1} - f_{t2}]W\tilde{\nu}$, where

$$f_{r1} = (1 + c_{r1})\frac{2r^*}{(1 + r^*)}\left[1 - c_{r3}\tan^{-1}(c_{r2}\tilde{r})\right] - c_{r1}, \tag{12}$$

and $c_{r1} = 1$, $c_{r2} = 12$. The constant c_{r3} has been assigned to be both 1.0 and 0.6 in Ref. 17, and Spalart and Shur admit that they are still experimenting with the function f_{r1}. In the current study, we use both values, and show that $c_{r3} = 0.6$ is the more appropriate choice for this case. The function r^* is given by $r^* = S/W$. The $\tilde{r}$ term is computed using

$$\tilde{r} = 2W_{ik}S_{jk}\left[\frac{DS_{ij}}{Dt} + (\epsilon_{imn}S_{jn} + \epsilon_{jmn}S_{in})\Omega_m\right]/D^4, \tag{13}$$

where the Ω_m term represents the system rotation, and $D = \sqrt{0.5(S^2 + W^2)}$. For 2-D flows and no system rotation, the expression for $\tilde{r}$ reduces to

$$\tilde{r} = -\left(\frac{D\alpha}{Dt}\right)\frac{8W_{12}(S_{11}^2 + S_{12}^2)}{D^4}, \tag{14}$$

with $D\alpha/Dt$ given by Eq. (9).

4 Results

In the experiment of So and Mellor,[2] the curved-wall tunnel had an aspect ratio of 8 (depth of 48 in.) and the flow along the tunnel centerline was nominally 2-D. Thus, 2-D computations are expected to adequately represent the flow field. The inner wall shape is defined by a series of 9 arc segments of varying angle and radius. The initial radius of curvature is 10 in., and the final radius of curvature is 13.86 in. The curved wall turns through a total of 150°. A detailed description of the inner wall shape can be found in So and Mellor.[2] The channel width is 6 in. at the inlet. An outer wall shape was obtained from the optimization program, which was run in Euler mode to obtain a shape such that the inner wall pressure distribution matched experiment throughout most of the curved region. A list of resulting outer wall points is given in Table 1. Inner wall points are given also, for reference.

The grid employed in the Navier-Stokes computations is shown in Fig. 1. The grid size is 257 × 161, with a minimum normal spacing at the convex wall of 0.00015 in. This corresponds with a spacing in wall coordinates of approximately $y^+ = 0.3$. The grid extends from 24 in. upstream of the curved wall

to approximately 18 in. downstream of the end of curvature. The Reynolds number per inch is taken as 3.6417×10^4, and the nominal Mach number at the inlet is $M = 0.063$. At the inflow boundary, the u-velocity profile is set based on the experimentally-measured skin friction and boundary layer thickness. The turbulence quantities are set to match the experimental levels at the same location. At the outflow boundary, pressure is specified at $p/p_{ref} = 1$, and all other quantities are extrapolated from the interior of the grid. Additional details concerning the boundary condition specifications can be found in Rumsey et al.[5]

Slip-wall boundary conditions are applied at the outer wall in the CFD simulation. This boundary condition is consistent with the assumption used in the optimization method, and allows the simulation to be run without the complication of having to contend with tangential jet or bleed boundary conditions. At the inner wall, standard no-slip adiabatic solid wall boundary conditions are employed.

For the remainder of the paper, we adopt a coordinate system with s measured along the inner wall in the flow direction and d measured normal to the inner wall. Thus, s represents the surface coordinates, or length measured along the inner wall surface. The boundary layer thickness at the inflow ($s = 24$ in.) is approximately 0.55 in., whereas at the start of the curvature ($s = 48$ in.) it is approximately 0.95 in. Thus, at the start of curvature, the parameter δ/R is roughly 0.095. According to Patel and Sotiropoulos,[20] $\delta/R < 0.01$ represents very mild curvature, whereas $0.1 < \delta/R < 1$ represents moderate to strong curvature. Therefore, the curvature for this case can probably be categorized as "moderate," whereas the Monson and Seegmiller U-duct case (with $\delta/R = 0.5$) can be categorized as "strong."[4,5]

In the experiment, the outer wall shape was set to allow a small pressure drop near the start of curvature, followed by a region of nearly constant pressure all the way to the end of the curved surface, at $s = 79.43$ in. Surface pressure coefficients are shown in Fig. 2 using two different turbulence models. The pressures match experiment very well over most of the inlet and curved wall segments.

The effect of grid density on a typical solution is shown in Figs. 3 and 4. In these figures, the "fine" level is the full 257×161 grid, "medium" has every other grid point removed in both directions, and "coarse" has every other grid point removed again. For this flow, the skin friction shows about a 3 - 5% difference between the coarse grid and fine grid solutions in the curved region, and roughly 1% difference (or less) between results on the medium and fine grids. The turbulent shear stress shows a difference between the coarse and medium levels, but no difference at all between the medium and fine levels. For all the remaining results in the paper, the medium level grid is employed.

The effect of the SARC model constant c_{r3} is shown in Fig. 5. Note that the c_f levels are referenced to the nominal velocity at the inlet, rather than the local "potential flow velocity at the wall," as reported in Ref. 2. The experimental levels have been adjusted accordingly. The original SA model yields high c_f levels over most of the curved-wall region. When SARC with $c_{r3} = 0.6$ is used, c_f levels agree well with experiment, but SARC with $c_{r3} = 1.0$ predicts c_f levels that are too low. Unless otherwise noted, for all remaining SARC results, a value for the constant $c_{r3} = 0.6$ is used.

Surface skin friction results using all four versions of the turbulence models are shown in Fig. 6. EASM and EASMCC are both low near the beginning of curvature but are relatively close to experimental levels over much of the curved-wall region beyond $s \approx 55$ in.; EASMCC reduces the c_f levels from that of EASM by only a modest amount. Overall, SARC, EASM, and EASMCC produce similar c_f levels over most of the curved region in reasonable agreement with experiment.

Velocity profiles in the bend are plotted in Fig. 7. In addition to results in the curved region, profiles are shown at the inlet ($s = 24$ in. station), although experimental data is not available at this location. As mentioned earlier, the velocity profile is set at the inflow to match the experimental c_f, δ, and nominal velocity using law-of-the-wall relations. As seen in the figure, initial profiles at the inlet are essentially identical for all four models. In the curved region, the results begin to differ. The three models SARC, EASM, and EASMCC are very close to each other and are in good agreement with experiment. However, the SA model predicts higher velocity levels over the first 20% of the boundary layer at all three stations.

Turbulent shear stress profiles are plotted in Fig. 8 for SA and SARC and in Fig. 9 for EASM and EASMCC. All shear and normal stress profiles, to be given below, are in the local body/normal coordinate system. Stresses in this frame are related to those in the Cartesian frame by the following relations:

$$\overline{u'v'} = \frac{1}{2}(\overline{v'v'}_c - \overline{u'u'}_c)\sin(2\Theta) + \overline{u'v'}_c\cos(2\Theta) \quad (15)$$

$$\overline{u'u'} = \overline{u'u'}_c\cos^2\Theta + \overline{v'v'}_c\sin^2\Theta + \overline{u'v'}_c\sin(2\Theta) \quad (16)$$

$$\overline{v'v'} = \overline{v'v'}_c \cos^2\Theta + \overline{u'u'}_c \sin^2\Theta - \overline{u'v'}_c \sin(2\Theta), \quad (17)$$

where the subscript c indicates Cartesian frame, and Θ is the angle that the body tangent vector makes with the x-axis. In Fig. 8, the SA model significantly overpredicts the $-\overline{u'v'}$ levels in the curved region, whereas SARC agrees much better with experiment. The differences between EASM and EASMCC in Fig. 9 are much less marked. However, EASMCC is generally in better agreement with experiment, particularly for $d/\delta > 0.3$, where the turbulence is suppressed to near-zero levels.

The turbulent normal stresses are plotted for EASM and EASMCC in Figs. 10 and 11. Because EASM and EASMCC are nonlinear models, they can predict the normal stress differences between $\overline{u'u'}$ and $\overline{v'v'}$. Results are in good agreement with experiment at the inflow and throughout the curvature region. The curvature correction in EASMCC has the effect of lowering the normal stress levels slightly from those of EASM. The $\overline{u'u'}$ and $\overline{v'v'}$ for SA and SARC are not shown. Linear eddy viscosity models cannot predict the normal stress differences, although the ability to predict these differences is generally not considered necessary for most thin shear flow applications.

Finally, the velocity profiles are shown using wall coordinates in Figs. 12 - 14. The theoretical log-law curve plotted in these figures is due to Spalding.[21] In the experimental results of Fig. 12, it is noted that the effect of curvature is primarily in the "wake" region beyond the log layer, where the u^+ levels are increased at successive stations downstream. The log layer itself remains unaffected by curvature. The SARC model overall reflects the correct trend, increasing u^+ in the wake region with downstream distance in the curve. However, the effect is excessive when $c_{r3} = 1.0$, and even the log layer itself is affected by the curvature correction and loses the correct slope. When $c_{r3} = 0.6$, a portion of the log layer retains the correct slope and only the region beyond $y^+ \approx 100$ is altered. The EASMCC model shows somewhat elevated wake levels of u^+, similar in character to the experiment, even with no curvature correction. These levels are raised slightly through the use of the curvature correction in EASMCC. In both EASM and EASMCC, the log layer remains in good agreement with the theoretical slope.

It is also instructive to return to check the original assumption made in the derivation of the EASMCC model. We already know from previous studies (e.g., Rumsey et al.[5]) that the assumption Eq. (4) is not valid in regions of high curvature. We would now like to investigate the validity of the transformed equation, Eq. (6). We do this by computing its actual value (the quantity $u_j \partial b_{ik}/\partial x_j$) at various locations in the converged solution, and comparing it to the quantity $b_{ik}\Omega_{kj} - \Omega_{ik}b_{kj}$.

Results are shown in Figs. 15 and 16 for Db_{11}/Dt and Db_{12}/Dt, respectively. The three successive curves in each figure represent results at the three stations in the curved region. It is shown in these figures that the assumption Eq. (6) is indeed valid in the curvature region, and is nearly exact in the lower part of the boundary layer.

5 Conclusions

This numerical study has yielded the following conclusions. The standard SA model (with no curvature correction) does not do a good job modeling the flow field with convex curvature. Eddy viscosity levels are significantly overpredicted, and velocity profiles are somewhat too full. The skin friction coefficient in the curved region is overpredicted. The curvature correction in SARC significantly improves results, lowering eddy viscosity levels and bringing velocity profiles into better agreement with experiment. The best choice for the model constant c_{r3} is 0.6 for this test case. A value of $c_{r3} = 1.0$ lowers the skin friction coefficient too much, and the log layers of the velocity profiles are significantly altered.

The EASM and EASMCC models both do a reasonably good job predicting this flow field. EASMCC has an advantage over SARC in that there are no heuristic functions and no additional constants necessary. The model is derived by assuming anisotropy equilibrium in the reference frame defined by the principal axes of the strain rate tensor, rather than in the Cartesian frame for standard EASM. The modified assumption on the anisotropy tensor is shown to be valid in the curved region of the flow field. However, the resulting curvature correction in EASMCC has only a minor effect for this case, slightly lowering the turbulent stress levels (in better agreement with experiment) and lowering the skin friction coefficient by a small amount. The effect on computed velocity profiles is very small.

Therefore it appears that some aspect of the EASM model enables it to perform reasonably well for this curved-flow case even without a curvature correction. Because the EASM is derived directly from the Reynolds stress model, it retains some of the invariance properties of the full differential form, even with the incorrect $Db_{ij}/Dt = 0$ assumption. Thus EASM yields a better physical representation of the turbulence than lower-order models such as SA. By including the curvature correction (in EASMCC), *all* the frame-invariance properties are retained. This modification does improve cer-

tain details in this flow field, but overall the effects are relatively minor.

Acknowledgments

The authors gratefully acknowledge W. K. Anderson, currently at Symantec Corporation, for his help in applying the adjoint optimization method to the So-Mellor configuration. The first author also wishes to thank P. R. Spalart of the Boeing Company and M. K. Strelets of the Federal Scientific Center of Applied Chemistry (Russia) for their assistance and helpful discussions.

References

1. Wilcox, D. W., Turbulence Modeling For CFD, 2nd Edition, DCW Industries, Inc., 1998.

2. So, R. M. C. and Mellor, G. L., "Experiment on Convex Curvature Effects in Turbulent Boundary Layers," *Journal of Fluid Mechanics*, Vol. 60, Part 1, 1973, pp. 43–62.

3. Gillis, J. C. and Johnston, J. P., "Turbulent Boundary-Layer Flow and Structure on a Convex Wall and its Redevelopment on a Flat Wall," *Journal of Fluid Mechanics*, Vol. 135, 1983, pp. 123–153.

4. Monson, D. J. and Seegmiller, H. L., "An Experimental Investigation of Subsonic Flow in a Two-Dimensional U-Duct," NASA TM 103931, July 1992.

5. Rumsey, C. L., Gatski, T. B., and Morrison, J. H., "Turbulence Model Predictions of Strongly-Curved Flow in a U-Duct," *AIAA Journal*, Vol. 38, No. 8, 2000, pp. 1394–1402.

6. Spalart, P. R., and Allmaras, S. R., "A One-Equation Turbulence Model for Aerodynamic Flows," *La Recherche Aerospatiale*, No. 1, 1994, pp. 5–21.

7. Menter, F. R., "Improved Two-Equation k-ω Turbulence Models for Aerodynamic Flows," NASA TM 103975, Oct. 1992.

8. Gatski, T. B., and Speziale, C. G., "On Explicit Algebraic Stress Models for Complex Turbulent Flows," *Journal of Fluid Mechanics*, Vol. 254, 1993, pp. 59–78.

9. Anderson, W. K. and Bonhaus, D. L., "Airfoil Design on Unstructured Grids for Turbulent Flows", *AIAA Journal*, Vol. 37, No. 2, 1999, pp. 185–191.

10. Nielsen, E. J. and Anderson, W. K., "Aerodynamic Design Optimization on Unstructured Meshes Using the Navier-Stokes Equations," *AIAA Journal*, Vol. 37, No. 11, 1999, pp. 1411–1419.

11. Wrenn, G. A., "An Indirect Method for Numerical Optimization Using the Kresselmeier-Steinhauser Function," NASA CR-4220, March 1989.

12. Krist S. L., Biedron R. T., and Rumsey C. L., "CFL3D User's Manual (Version 5.0)", NASA TM-1998-208444, June 1998.

13. Gatski, T. B., and Rumsey, C. L., "Linear and Non-Linear Eddy Viscosity Models," Closure Strategies for Turbulent and Transitional Flows (B. E. Launder and N. D. Sandham, eds.), Cambridge University Press, To Appear, 2001.

14. Schunk, P. R. and Scriven, L. E., "Constitutive Equation for Modeling Mixed Extension and Shear in Polymer Solution Processing," *J. Rheology*, Vol. 34, 1990, pp. 1085–1119.

15. Souza Mendes, P. R., Padmanabhan, M., Scriven, L. E., and Macosko, C. W., "Inelastic Constitutive Equations for Complex Flows," *Rheol. Acta*, Vol. 34, 1995, pp. 209–214.

16. Speziale, C. G., Sarkar, S., and Gatski, T. B., "Modeling the Pressure-Strain Correlation of Turbulence: an Invariant Dynamical Systems Approach," *J. Fluid Mech.*, Vol. 227, 1991, pp. 245–272.

17. Spalart, P.R., and Shur, M., "On the Sensitization of Turbulence Models to Rotation and Curvature," *Aerospace Science and Technology*, No. 5, 1997, pp. 297–302.

18. Shur, M., Strelets, M., Travin, A., and Spalart, P.R., "Turbulence Modeling in Rotating and Curved Channels: Assessing the Spalart-Shur Correction," *AIAA Journal*, Vol. 38, No. 5, 2000, pp. 784–792.

19. Patel, V. C., and Sotiropoulos, F., "Longitudinal Curvature Effects in Turbulent Boundary Layers," *Prog. Aerospace Sci.*, Vol. 33, 1997, pp. 1–70.

20. White, F. M., Viscous Fluid Flow, McGraw-Hill, Inc., New York, 1974.

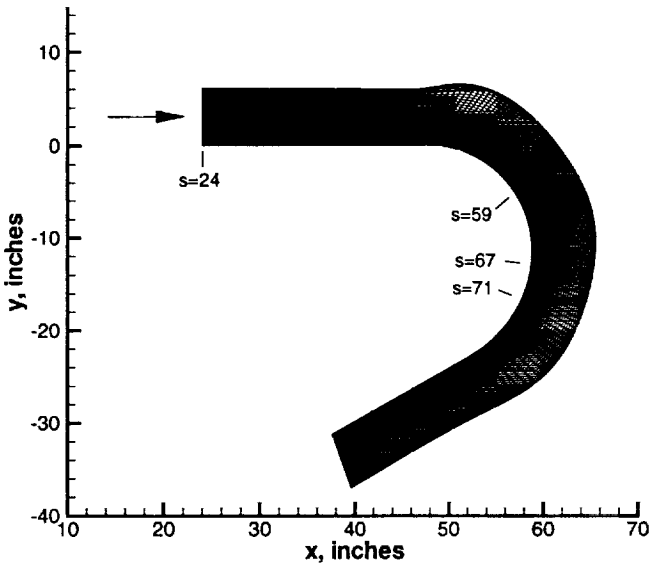

Figure 1. Grid for So-Mellor case, every other point of 257 × 161 grid shown.

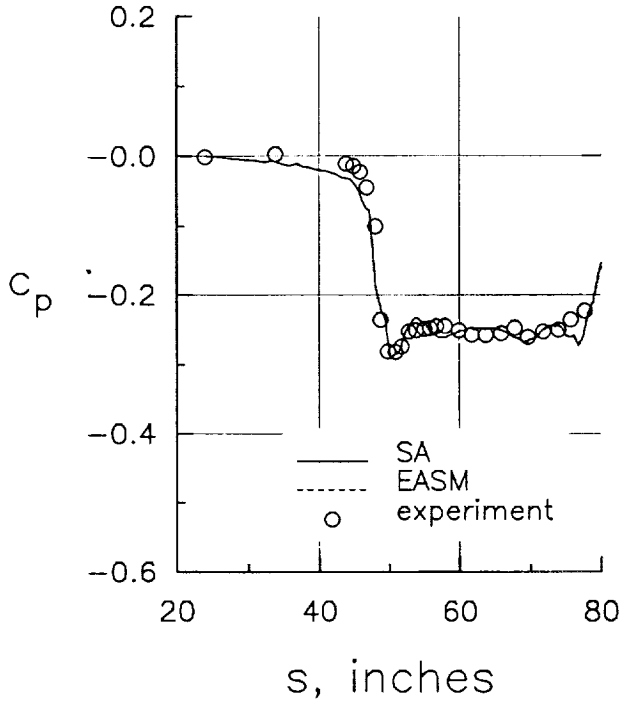

Figure 2. Surface pressure coefficient, referenced to inlet conditions.

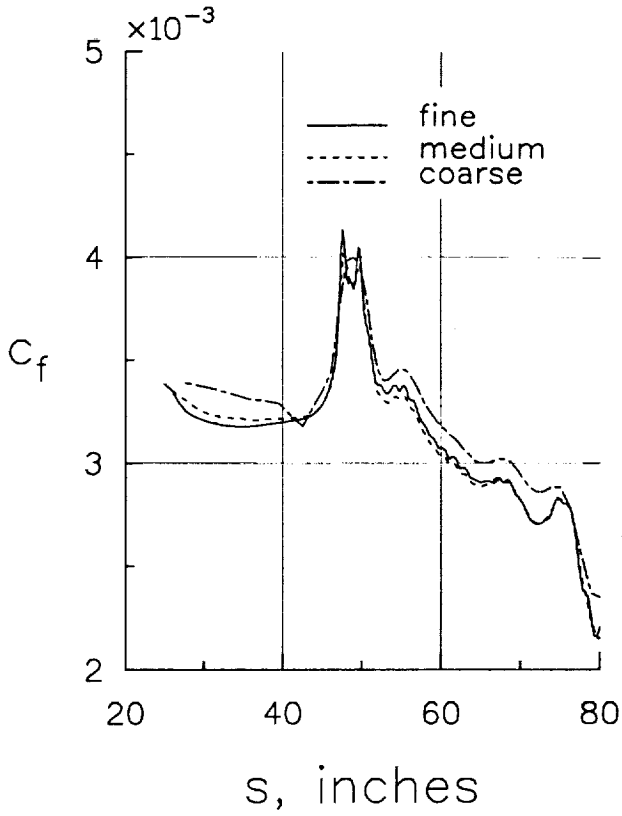

Figure 3. Effect of grid size on surface skin friction coefficient, EASMCC model.

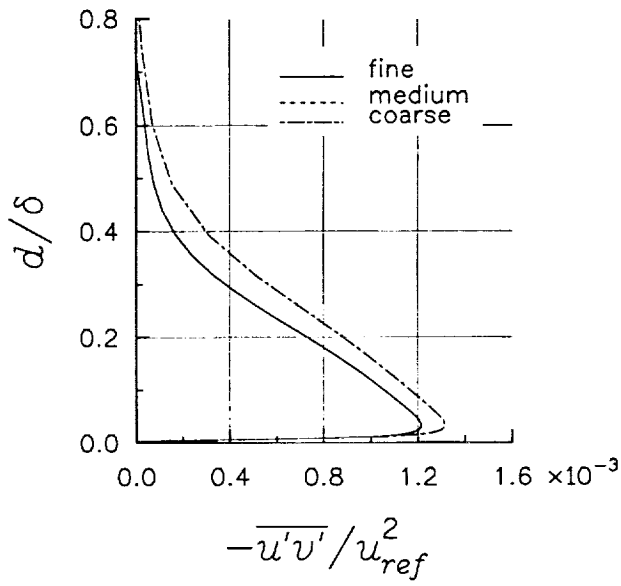

Figure 4. Effect of grid size on turbulent shear stress profile at $s = 71$ in., EASMCC model (fine and medium curves are indistinguishable).

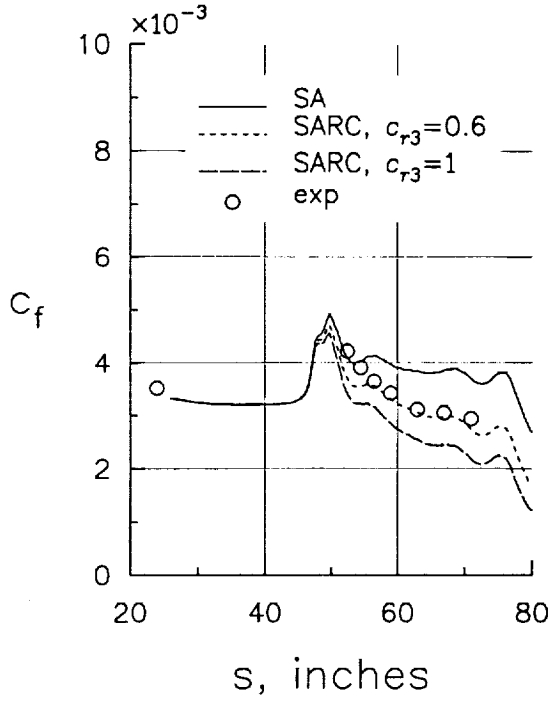

Figure 5. Effect of SARC model constant on surface skin friction coefficient, referenced to inlet conditions.

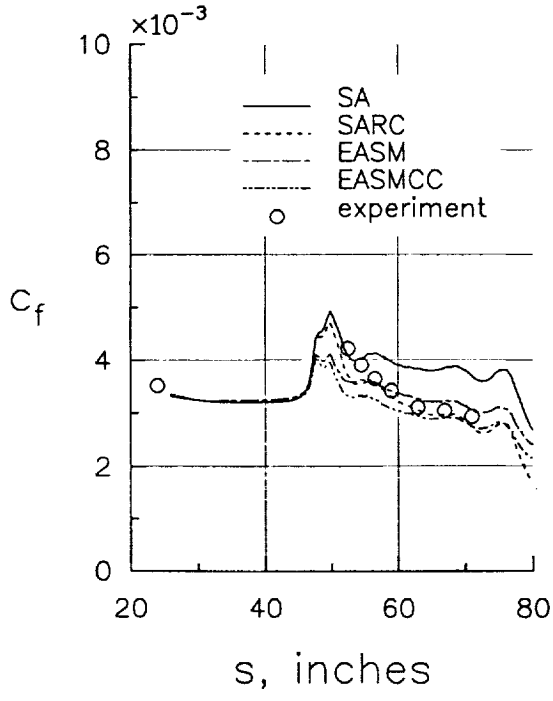

Figure 6. Surface skin friction coefficient, referenced to inlet conditions.

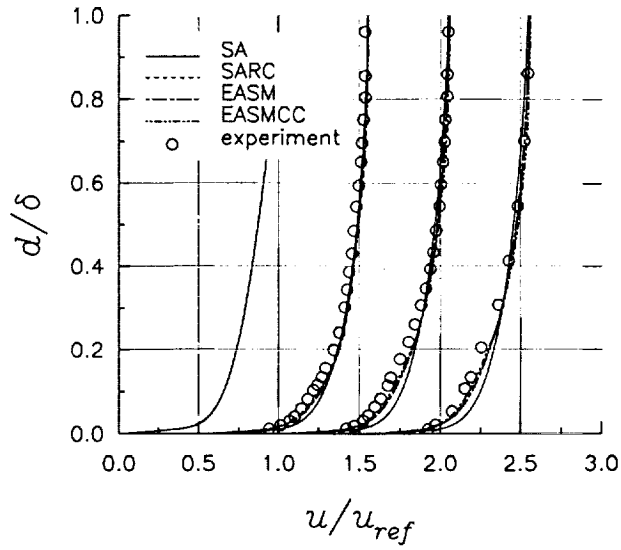

Figure 7. Velocity profiles at $s = 24$ in., $s = 59$ in., $s = 67$ in., and $s = 71$ in., referenced to inlet conditions (origin for each successive station is shifted 0.5 units to the right).

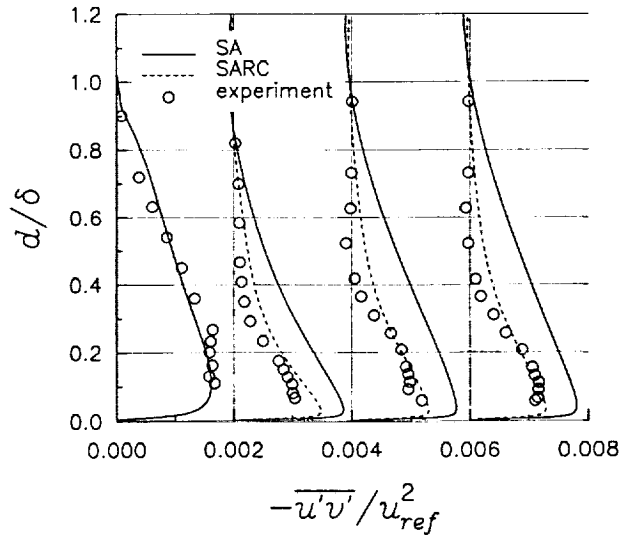

Figure 8. Turbulent shear stress profiles for the SA and SARC models at $s = 24$ in., $s = 59$ in., $s = 67$ in., and $s = 71$ in., referenced to inlet conditions (origin for each successive station is shifted 0.002 units to the right).

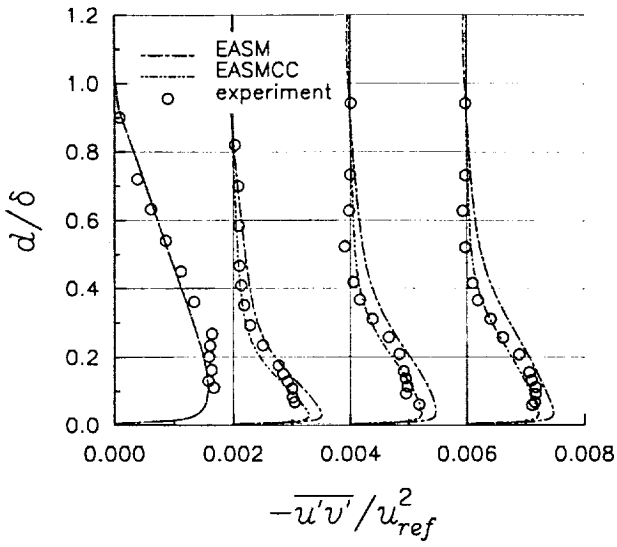

Figure 9. Turbulent shear stress profiles for the EASM and EASMCC models at $s = 24$ in., $s = 59$ in., $s = 67$ in., and $s = 71$ in., referenced to inlet conditions (origin for each successive station is shifted 0.002 units to the right).

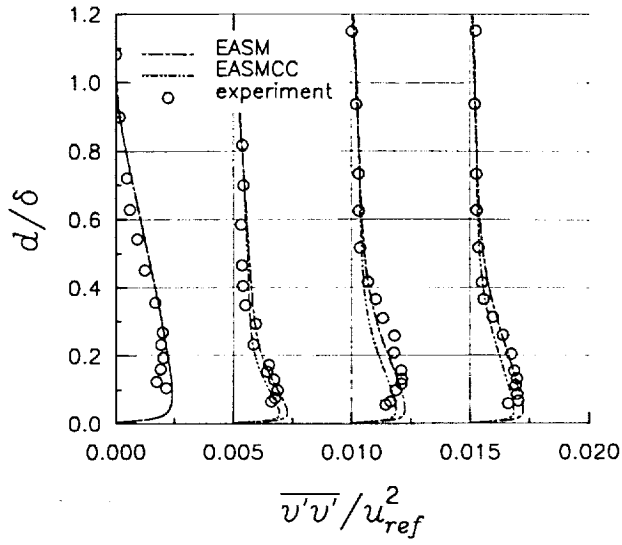

Figure 11. $\overline{v'v'}$ turbulent normal stress profiles for the EASM and EASMCC models at $s = 24$ in., $s = 59$ in., $s = 67$ in., and $s = 71$ in., referenced to inlet conditions (origin for each successive station is shifted 0.005 units to the right).

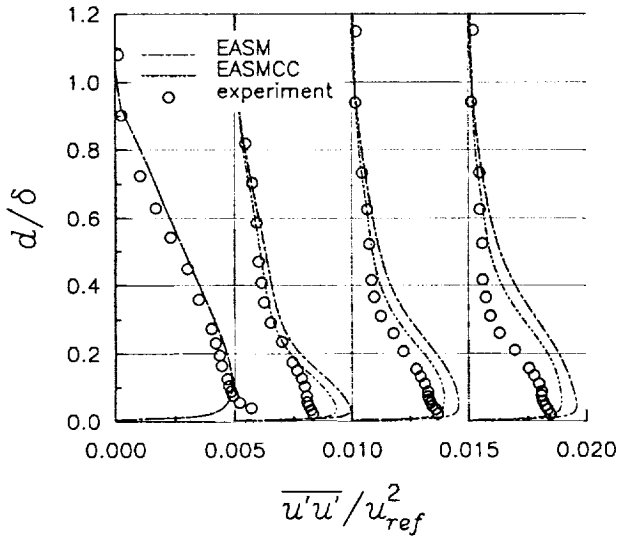

Figure 10. $\overline{u'u'}$ turbulent normal stress profiles for the EASM and EASMCC models at $s = 24$ in., $s = 59$ in., $s = 67$ in., and $s = 71$ in., referenced to inlet conditions (origin for each successive station is shifted 0.005 units to the right).

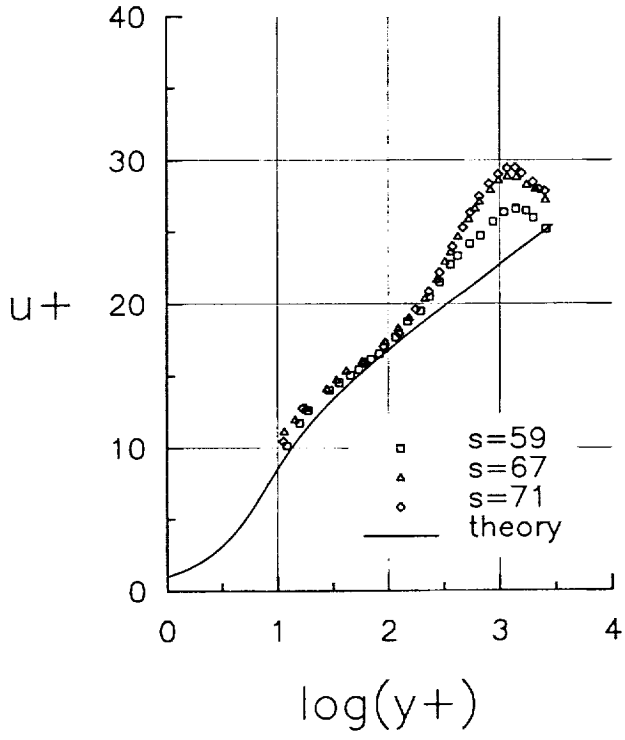

Figure 12. Semi-log plot of the experimental velocity profiles.

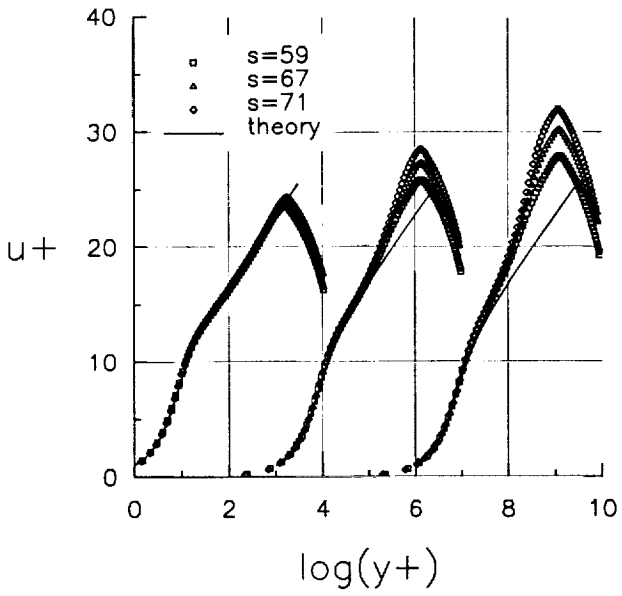

Figure 13. Semi-log plot of the velocity profiles for SA and SARC (SARC with $c_{r3} = 0.6$ is shifted 3 units to the right, and SARC with $c_{r3} = 1.0$ is shifted 6 units to the right).

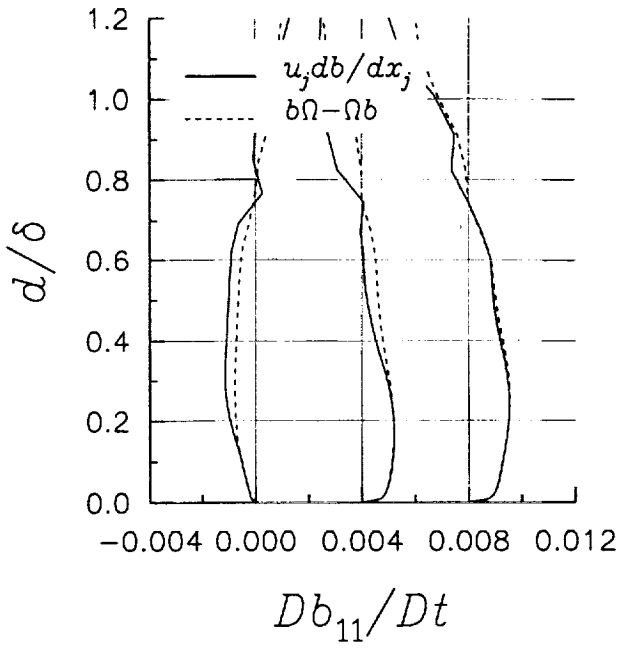

Figure 15. Comparison of actual Db_{11}/Dt with EASMCC assumption at $s = 59$ in., $s = 67$ in., and $s = 71$ in. (origin for each successive station is shifted 0.004 units to the right).

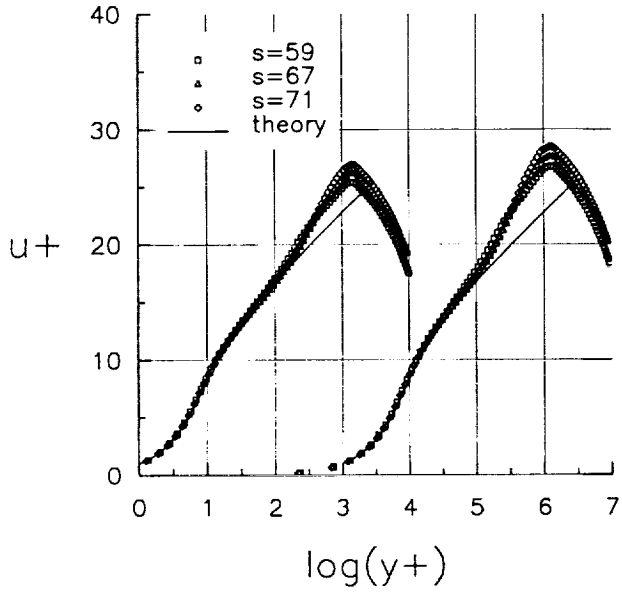

Figure 14. Semi-log plot of the velocity profiles for EASM and EASMCC (EASMCC is shifted 3 units to the right).

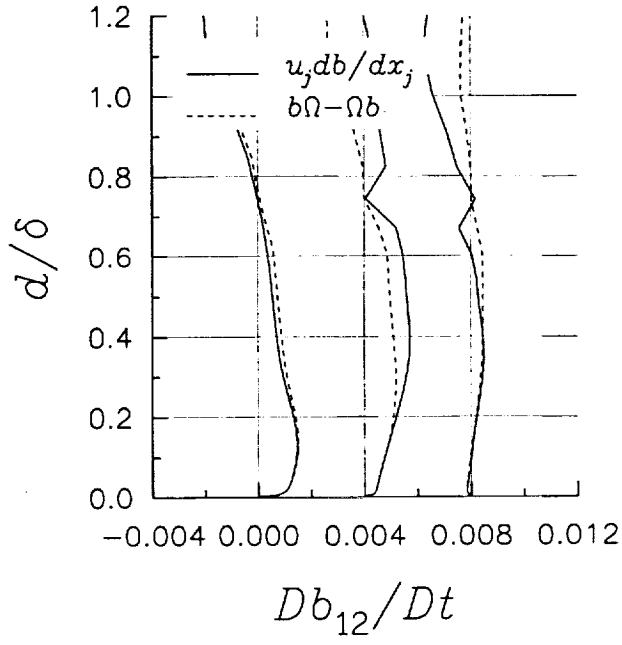

Figure 16. Comparison of actual Db_{12}/Dt with EASMCC assumption at $s = 59$ in., $s = 67$ in., and $s = 71$ in. (origin for each successive station is shifted 0.004 units to the right).

Table 1. Wall points (in.) used for So-Mellor case

xinner	yinner	xouter	youter
.2400E+02	.0000E+00	.2400E+02	.6000E+01
.3350E+02	.0000E+00	.3406E+02	.6000E+01
.3580E+02	.0000E+00	.3668E+02	.6004E+01
.3780E+02	.0000E+00	.3905E+02	.5983E+01
.3957E+02	.0000E+00	.4119E+02	.5969E+01
.4116E+02	.0000E+00	.4315E+02	.5954E+01
.4258E+02	.0000E+00	.4495E+02	.5958E+01
.4388E+02	.0000E+00	.4661E+02	.5978E+01
.4506E+02	.0000E+00	.4815E+02	.6171E+01
.4615E+02	.0000E+00	.4957E+02	.6390E+01
.4716E+02	.1652E-02	.5092E+02	.6508E+01
.4810E+02	-.5451E-02	.5220E+02	.6466E+01
.4898E+02	-.6397E-01	.5339E+02	.6254E+01
.4980E+02	-.1668E+00	.5448E+02	.5904E+01
.5057E+02	-.3273E+00	.5548E+02	.5456E+01
.5128E+02	-.5392E+00	.5639E+02	.4941E+01
.5194E+02	-.7944E+00	.5723E+02	.4379E+01
.5255E+02	-.1081E+01	.5799E+02	.3784E+01
.5313E+02	-.1391E+01	.5870E+02	.3165E+01
.5366E+02	-.1721E+01	.5935E+02	.2530E+01
.5416E+02	-.2067E+01	.5995E+02	.1886E+01
.5462E+02	-.2428E+01	.6051E+02	.1236E+01
.5506E+02	-.2802E+01	.6104E+02	.5848E+00
.5546E+02	-.3189E+01	.6155E+02	-.6808E-01
.5584E+02	-.3588E+01	.6202E+02	-.7222E+00
.5619E+02	-.3999E+01	.6248E+02	-.1379E+01
.5651E+02	-.4419E+01	.6290E+02	-.2040E+01
.5682E+02	-.4849E+01	.6331E+02	-.2707E+01
.5710E+02	-.5288E+01	.6369E+02	-.3382E+01
.5736E+02	-.5737E+01	.6404E+02	-.4069E+01
.5759E+02	-.6195E+01	.6435E+02	-.4768E+01
.5781E+02	-.6663E+01	.6464E+02	-.5480E+01
.5801E+02	-.7142E+01	.6489E+02	-.6209E+01
.5819E+02	-.7631E+01	.6510E+02	-.6953E+01
.5835E+02	-.8133E+01	.6528E+02	-.7713E+01
.5848E+02	-.8646E+01	.6541E+02	-.8490E+01
.5860E+02	-.9173E+01	.6550E+02	-.9282E+01
.5869E+02	-.9714E+01	.6554E+02	-.1009E+02
.5876E+02	-.1027E+02	.6554E+02	-.1091E+02
.5880E+02	-.1084E+02	.6550E+02	-.1175E+02
.5881E+02	-.1143E+02	.6542E+02	-.1261E+02
.5880E+02	-.1204E+02	.6530E+02	-.1348E+02
.5876E+02	-.1266E+02	.6514E+02	-.1438E+02
.5868E+02	-.1331E+02	.6495E+02	-.1529E+02
.5856E+02	-.1398E+02	.6471E+02	-.1623E+02
.5840E+02	-.1467E+02	.6443E+02	-.1720E+02
.5819E+02	-.1538E+02	.6411E+02	-.1820E+02
.5793E+02	-.1612E+02	.6373E+02	-.1923E+02
.5760E+02	-.1688E+02	.6327E+02	-.2028E+02
.5719E+02	-.1766E+02	.6273E+02	-.2136E+02
.5671E+02	-.1847E+02	.6208E+02	-.2246E+02

xinner	yinner	xouter	youter
.5613E+02	-.1929E+02	.6129E+02	-.2356E+02
.5544E+02	-.2014E+02	.6033E+02	-.2464E+02
.5462E+02	-.2099E+02	.5918E+02	-.2567E+02
.5363E+02	-.2182E+02	.5782E+02	-.2663E+02
.5246E+02	-.2263E+02	.5627E+02	-.2756E+02
.5110E+02	-.2345E+02	.5454E+02	-.2846E+02
.4957E+02	-.2433E+02	.5263E+02	-.2944E+02
.4783E+02	-.2533E+02	.5055E+02	-.3056E+02
.4584E+02	-.2647E+02	.4826E+02	-.3185E+02
.4354E+02	-.2780E+02	.4572E+02	-.3332E+02
.4084E+02	-.2935E+02	.4288E+02	-.3505E+02
.3761E+02	-.3122E+02	.3962E+02	-.3699E+02